Polymer Testing 108 (2022) 107512

Contents lists available at ScienceDirect

Polymer Testing

journal homepage: www.elsevier.com/locate/polytest

Displacement rate effects on mixed-mode I/II delamination of laminated carbon/epoxy composites

Kean Ong Low [a,b], Mahzan Johar [c], Aun Naa Sung [d], Mohd Nazri Mohd Nasir [a], Seyed Saeid Rahimian Koloor [e,f,*], Michal Petrů [g], Haris Ahmad Israr [a], King Jye Wong [a,**]

[a] School of Mechanical Engineering, Faculty of Engineering, Universiti Teknologi Malaysia, 81310, Johor Bahru, Malaysia
[b] Faculty of Engineering and Technology, Multimedia University, Jalan Ayer Keroh Lama, 75450, Melaka, Malaysia
[c] Quality Engineering Research Cluster QEREC, Quality Engineering Section, Malaysian Institute of Industrial Technology, Universiti Kuala Lumpur, Masai, Johor, Malaysia
[d] Faculty of Engineering and Science, Curtin University Malaysia, 98009, Miri, Malaysia
[e] Institute for Nanomaterials, Advanced Technologies and Innovation CXI, Technical University of Liberec TUL, Studentska 2, 461 17, Liberec, Czech Republic
[f] Department of Aerospace Engineering, Faculty of Engineering, Universiti Putra Malaysia, Serdang, 43400, Malaysia
[g] Technical University of Liberec TUL, Studentska 2, 461 17, Liberec, Czech Republic

ARTICLE INFO

Keywords:
Carbon/epoxy composite
Rate dependence
Mixed-mode delamination
Fractography
Cohesive zone modelling

ABSTRACT

Mixed-mode delamination is one of the common failures of composites which has not been studied under low-impact loading. This paper studies the influence of displacement rate on mixed-mode I/II delamination of unidirectional carbon/epoxy composites. Single leg bending test is performed at displacement rates of 1, 10, 100, and 500 mm/min. Experimental results reveal that the mixed-mode I/II fracture toughness is invariant with the displacement rate. In addition, scanning electron micrographs shows that shear cusps are more obvious at 1, 10, and 100 mm/min. At 500 mm/min, significant matrix debris is noticed. Furthermore, the proposed three-dimensional rate-dependent fracture criterion is found to well predict the fracture toughness. Numerical simulation using cohesive zone model suggests that the lower numerical peak load is due to lower damage dissipated energy. In addition, the theoretical and numerical traction-separation responses show significant differences, which is also reflected in the numerical phase angle. This implies that the local mixed-mode ratio is not constant throughout the simulation process.

1. Introduction

Delamination is one of the major failure mechanisms in composite laminates due to low interlaminar strength [1–3]. Therefore, researchers have been trying to improve the interlaminar properties. For example, Hosseini et al. [4,5] investigated the mode I and mode II delamination of twill woven E-glass/L20 epoxy composite laminates using double cantilever beam (DCB) and end-notched flexure (ENF) specimens, respectively. Comparison was made between composites with and without the glass fibre chopped strand mat layers. The intention of using the mat-interlayer was to avoid through thickness crack development and reduce the possibility of catastrophic failure in the composite structures. Results revealed that for both mode I and mode II cases, the specimens without mat-interlayer have attained higher initiation and propagation fracture toughness values as compared to the specimens with mat-interlayer reinforcement. Not only that, by using exponential-linear traction separation model, the numerical and experimental force-displacement curves for the DCB test specimens were well compared. In addition, as the loadings are generally complex in reality [6] and polymeric materials are commonly known to be rate-dependent [7,8], it is essential to understand the influence of loading speed on mixed-mode I/II delamination behaviour of composite laminates.

In the literature, the studies on the speed dependence on the delamination of composite materials are mainly focusing on mode I and

* Corresponding author. Institute for Nanomaterials, Advanced Technologies and Innovation CXI, Technical University of Liberec TUL, Studentska 2, 461 17, Liberec, Czech Republic.
** Corresponding author.
E-mail addresses: kolow@mmu.edu.my (K.O. Low), mahzan@unikl.edu.my (M. Johar), sung.aun@curtin.edu.my (A.N. Sung), mnazrimnasir@utm.my (M.N. Mohd Nasir), s.s.r.koloor@gmail.com (S.S. Rahimian Koloor), michal.petru@tul.cz (M. Petrů), haris@mail.fkm.utm.my (H.A. Israr), kjwong@mail.fkm.utm.my (K.J. Wong).

https://doi.org/10.1016/j.polymertesting.2022.107512
Received 4 November 2021; Received in revised form 16 January 2022; Accepted 9 February 2022
Available online 12 February 2022

mode II cases. For instance, Machado et al. [9,10] studied the temperature and displacement rate effects on mode I and mode II delamination behaviour of unidirectional carbon/epoxy composites. Experiments were conducted at 2 mm/min and 100 mm/min. Results showed that both mode I (G_{IC}) and mode II (G_{IIC}) fracture toughnesses at all temperatures (−30 °C, 20 °C, and 80 °C) decreased with the loading rate. Zabala et al. [11,12] tested unidirectional carbon/epoxy composite within the loading rate of 5 mm/min – 0.19 m/s. Similarly, a decrement in G_{IC} was reported. However, G_{IIC} was found to be invariant with the loading rate. On the other hand, Marzi et al. [13] discovered that by testing the carbon-reinforced polymer composite at 0.05 mm/s and 100 mm/s, a decrement in G_{IC} but negligible variation in G_{IIC} were reported. Not only that, Colin de Verdiere et al. [14,15] investigated the delamination behaviour of untufted and carbon thread tufted carbon non crimp fabric (NCF)/epoxy up to 8.7 m/s for mode I and 7 m/s for mode II. Both G_{IC} and G_{IIC} were noticed to be invariant for untufted composite. However, for tufted composite, G_{IC} was invariant while G_{IIC} increased with the loading rate.

Compared to mode I and mode II delamination, the research on the rate-dependency of mixed-mode I/II delamination is still very limited. For example, Blackman et al. [16,17] investigated both unidirectional carbon/epoxy and carbon/PEEK composites. The imposed loading rates were up to 15 m/s for mode I and 5 m/s for mode II and mixed-mode I/II loadings. It was found that all G_{IC}, G_{IIC}, and mixed-mode $G_{I/IIC}$ fracture toughnesses appeared to be invariant with the loading rate in the carbon/epoxy composite. As for carbon/PEEK, they decreased with loading rate at all modes.

From the abovementioned literature, it could be deduced that the influence of loading rate on the delamination behaviour of composite materials is still not conclusive. In addition to the types of material, the difference could also be due to the difficulty in obtaining the load signal [16] and test setup [7,14,18]. Furthermore, there are very limited works reported on mixed-mode I/II. Mixed-mode delamination is important to be considered due to complex loadings in nature. For example, Esmaili and Taheri-Behrooz [19] proposed a novel model to estimate the cohesive zone length (CZL) under fatigue-induced mixed-mode I/II delamination. The modified CZL considers both the material and structural geometry effects. Results showed a more accurate prediction of the crack growth rate in the Paris curve compared with the experimental data obtained from the literature. Their results highlighted the importance of the cohesive zone behind the crack tip. Rafiee and Sotoudeh [20] developed a new cohesive zone model for mixed-mode delamination. The irreversible interface degradation under cyclic loading was considered through the introduction of a new damage parameter, where the interlaminar stiffness reduction was expressed as a function of tractions, interfacial strength properties and coupled with the parameters of the mixed-mode bilinear traction-separation law. In their subsequent publication, the authors fabricated unidirectional glass fibre reinforced epoxy composite laminates using hand layup and vacuum infusion process (VIP) [21]. The composites were fabricated at three stacking sequences: $[0_{12}]$, $[(0/\pm45)_4]$ and $[\pm45_6]$. Fatigue tests were carried out on double cantilever beam test specimens under displacement control, at a fixed load ratio, R = 0.1 up to 10^4 cycles. The authors implemented the new cohesive zone model that was developed previously [20] to simulate the fatigue delamination onset of the composites. The numerical results revealed a good agreement with the experimental data. In addition, Rafiee and Sotoudeh [22] have also successfully implemented the model to simulate the mode II delamination onset of IM7/8552 carbon/epoxy composite using double-notch shear (DNS) test specimen results by May and Hallett [23]. In view of this, it is necessary to further investigate the loading rate effects on the mixed-mode I/II delamination.

In the authors' previous works, the displacement rate effects on mode I [24] and mode II [25] delamination of unidirectional carbon/-epoxy composites have been studied. It was interesting to find that within the crosshead displacement rates of 1–500 mm/min, mode I fracture toughness is independent of the displacement rate [24], while the displacement rate has a positive effect on the mode II fracture toughness [25]. Considering the different observations in both mode I and mode II delamination behaviour; and noting that the loadings in real life applications are usually complex, this paper continues the characterisation of the displacement rate effects on mixed-mode I/II delamination behaviour of the same unidirectional carbon/epoxy composites. Single leg bending (SLB) test was conducted at displacement rates of 1, 10, 100, and 500 mm/min. The mixed-mode fracture toughness was calculated using the compliance calibration (CC) method. Subsequently, the delaminated surfaces were analysed through the scanning electron microscope. After that, a three-dimensional rate-dependent model was proposed. Finally, the delamination behaviour was simulated using a cohesive zone model. Comparisons were done on the force-displacement curve, crack growth profile, traction-separation response, phase angle, and fracture energy.

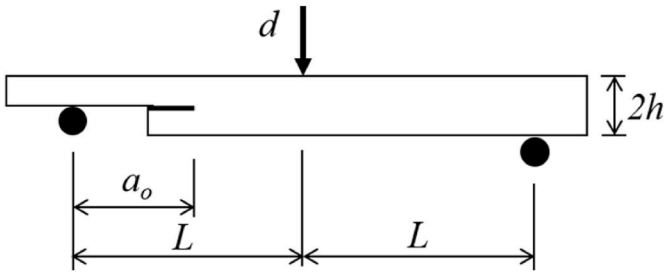

Fig. 1. Schematic diagram of SLB test setup.

2. Materials and methods

2.1. Materials and specimens

The unidirectional carbon/epoxy prepreg used in this research has a nominal ply thickness of 0.15 mm [24,25]. The epoxy resin is Bisphenol A cured by dicyandiamide, while the carbon fibre is unidirectional with 150 gsm. The average fibre volume fraction is 65.7 ± 6.3%, while the carbon fibre has an average diameter of 6.8 μm. Firstly, a unidirectional composite plate with $[0]_{20}$ was fabricated using the hand lay-up technique. To generate the pre-crack, a 15 μm Teflon film was placed at the mid-thickness location of the plate. The composite was then hot-pressed and has an average thickness ($2h$) of 3 mm upon curing. After that, it was cut into specimens of 20 mm width using a computer numerical control (CNC) machine. All specimens were prepared and supplied by "X Plas Singapore".

2.2. Interlaminar fracture toughness test

Mixed-mode I/II delamination was achieved through the single-leg bending (SLB) test (Fig. 1). SLB test was carried out at displacement rates of 1, 10, 100, and 500 mm/min. This was categorised as the low-speed range [26]. All tests were displacement controlled using Instron Universal Testing Machine 5982 with a load cell capacity of 5 kN. At least three specimens were tested for each displacement rate. All tests were performed at ambient conditions.

2.3. Morphology study

The delaminated surfaces were gold-coated by 134 Bio-Rad Polaron Division before SEM images were taken using scanning electron microscope Philips XL40.

3. Data reduction method

The calculation of the fracture toughness $G_{I/IIC}$ is based on the Irwin-

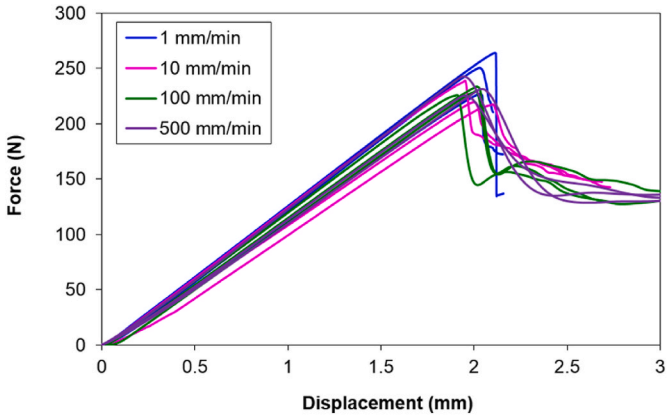

Fig. 2. Force-displacement curves of the SLB specimens at all displacement rates.

Kies [27] equation:

$$G_C = \frac{P_C^2}{2B}\left(\frac{dC}{da}\right) \tag{1}$$

where P_C is the critical load, B is the width of the specimen, C is the compliance (inverse of the initial linear slope) and a is the crack length. The compliance calibration model is written as:

$$C = C_2 a^3 + C_1 \tag{2}$$

In Eq. (2), C_2 and C_1 are obtained through the fitting of $C - a^3$ plot. Substituting the derivative of Eq. (2) into Eq. (1) yields:

$$G_C = \frac{P_C^2}{2B} \cdot 3C_2 a^2 \tag{3}$$

The initial crack length was fixed at 30 mm for all displacement rates. In order to generate the compliance plot, additional specimens were tested at crack lengths of 20, 25, 35, and 40 mm within the linear region.

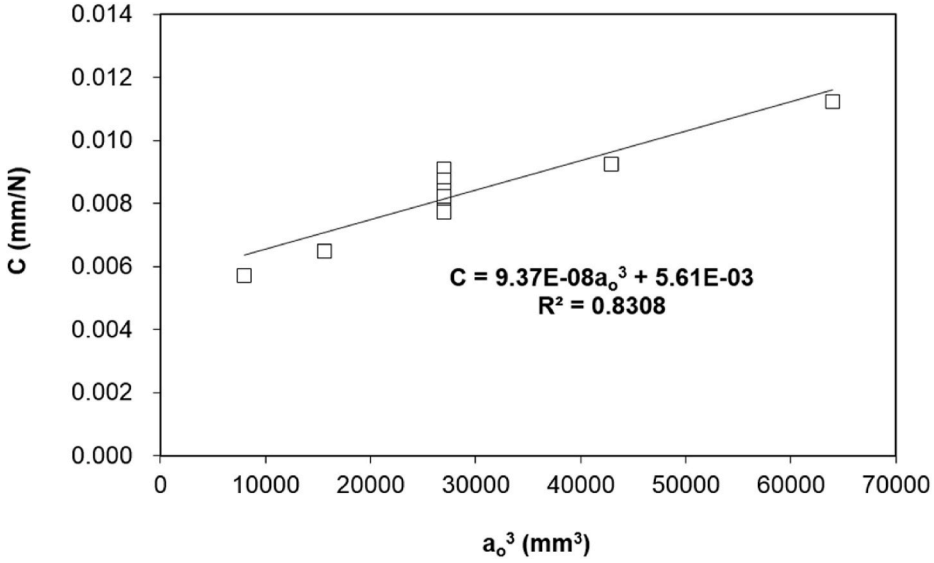

Fig. 3. Compliance plot of the SLB test at different crack lengths.

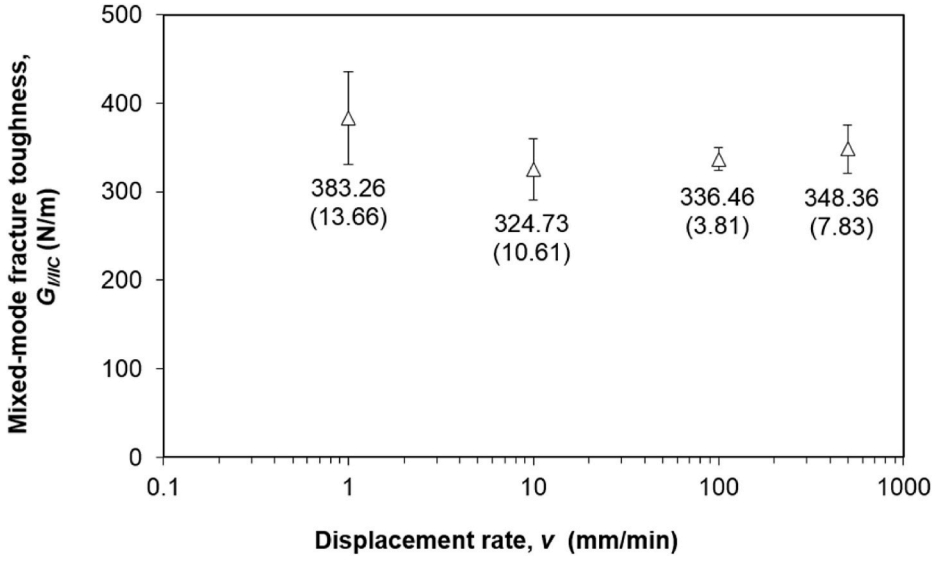

Fig. 4. Mixed-mode I/II fracture toughness at various displacement rates.

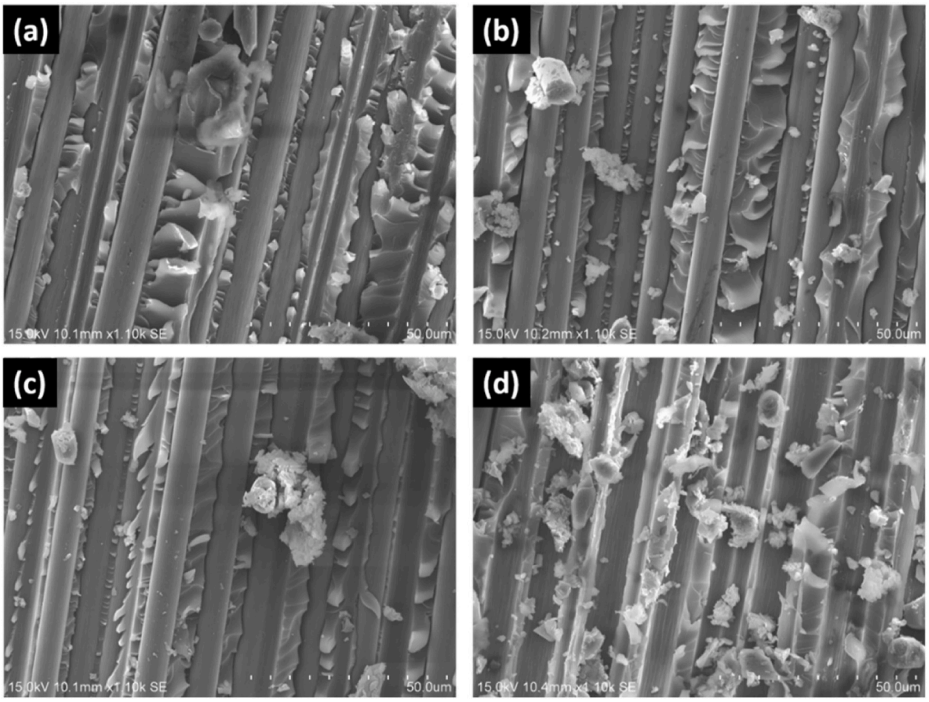

Fig. 5. Scanning electron micrographs of the SLB specimens at (a) 1, (b) 10, (c) 100, and (d) 500 mm/min.

4. Results and discussion

4.1. Force-displacement curves

Fig. 2 shows the force-displacement curves of the SLB specimens at displacement rates of 1, 10, 100, and 500 mm/min. During the early stage of loading, the force increases linearly with the imposed displacement. When the peak force is attained, the force drops abruptly. This indicates unstable crack growth. At all displacement rates, the slopes at the initial region are close to each other, where the average slopes are 123, 119, 122, and 123 N/mm for 1, 10, 100, and 500 mm/min. By using the average slope at 1 mm/min as a reference, the maximum difference between them is only approximately 3%. This implies that within 1–500 mm/min, the stiffness of this composite is not sensitive to the displacement rate. A similar observation was reported for mode I and mode II tests on the same carbon/epoxy composite material [24,25]. This is also similar to the observation by Cantwell [28], which was been highlighted by Yasaee et al. [29] as well.

4.2. Mixed-mode I/II fracture toughness

Fig. 3 depicts the compliance plot of the SLB test tested at 1 mm/min, where the best fit parameters are $C_2 = 9.37 \times 10^{-8}$ mm^{-2} N^{-1} and $C_1 = 5.61 \times 10^{-3}$ mm N^{-1}, with $R^2 = 0.8308$. The same C_2 value is used to compute the fracture toughness of each test at all displacement rates. This is based on the previous observation in Fig. 2, where the stiffness is similar at all displacement rates. The average fracture toughness values are listed in Fig. 4, with the values in the bracket referring to the coefficient of variation in %. Based on the results, the mixed-mode I/II fracture toughness $G_{I/IIC}$ is found to be invariant with the displacement rate. Compared to $G_{I/IIC}$ at 1 mm/min, the difference is 15%, 4% and 4% at 10, 100 and 500 mm/min, respectively.

The scanning electron micrographs are captured at the mid-width crack tip location of the specimen. Fig. 5 (a)–(c) shows that the fractography of the SLB specimens at 1, 10, and 100 mm/min are similar. Firstly, shear cusps are observed, which is an indication of the mode II component, and is widely noticed in brittle matrix composites [29–36].

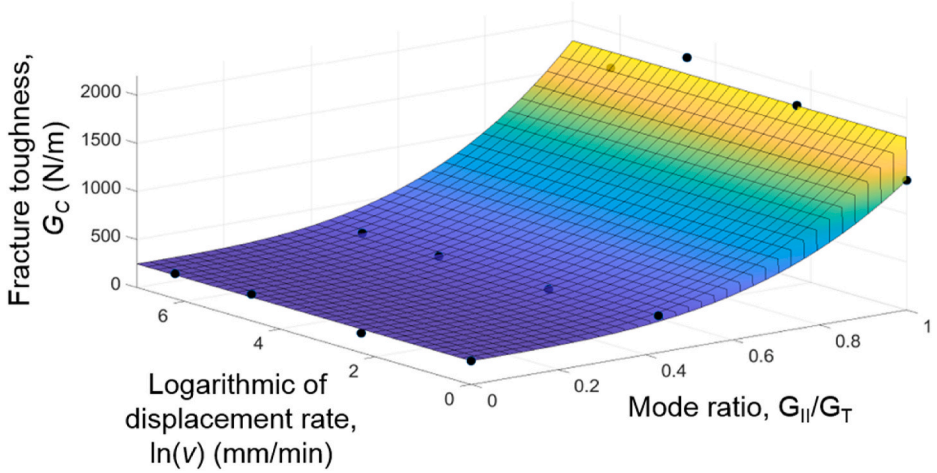

Fig. 6. Three-dimensional presentation of the experimental data and best-fit surface plot.

Table 1
Absolute percentage deviation of fracture toughness obtained from experiment and curve fitting.

Mode ratio	Displacement rate in In scale	Experimental fracture toughness, FT_e	Curve fit fracture toughness, FT_c	Absolute percentage deviation of fracture toughness, ΔFT
0	0	245.03	245.00	0%
0.43	0	383.26	320.72	16%
1	0	1349.26	1349.00	0%
0	2.3	202.59	245.00	21%
0.43	2.3	324.73	351.17	8%
1	2.3	1795.78	1792.87	0%
0	4.6	275.06	245.00	11%
0.43	4.6	336.46	351.17	4%
1	4.6	1962.69	1792.91	9%
0	6.2	258.59	245.00	5%
0.43	6.2	348.36	351.17	1%
1	6.2	1623.85	1792.93	10%
Average percentage deviation				7%

Secondly, the existence of clean fibre surfaces implies the adhesive failure of the fibre/matrix interface, which is an indication of weak fibre/matrix interfacial bonding [32,37]. Thirdly, matrix cracking is also noticed, despite it is not significant. At 500 mm/min, Fig. 5 (d) shows different observation, where there is less shear cusps but more matrix debris.

4.3. Three-dimensional plot of the fracture toughness

Combining the results on mode I [24], mode II [25], and mixed-mode I/II, Fig. 6 plots the experimental fracture toughness (marked as "●") in three-dimensional form. It is to note that only mode II fracture toughness was found to be sensitive to the displacement rate [25] and could be fitted using:

$$G_{IIC}(v) = G_{IIC,QS}\left\{1 + m\left[\ln\left(\frac{v}{v_{QS}}\right)\right]^{\zeta}\right\} \tag{4}$$

where $G_{IIC}(v)$ refers to the mode II fracture toughness at loading speed v and the subscript QS indicates the G_{IIC} at the lowest displacement rate (1 mm/min). The best-fit parameters of m and ζ were found to be 3.29×10^{-1} and 1.36×10^{-4} [25]. In this study, the variation of the fracture toughness as a function of displacement rate is therefore proposed to be fitted using the modified BK-criterion:

Table 2
Lamina properties for the carbon/epoxy composite used in this study [24,25].

E_{11} (GPa)	E_2 (GPa)	G_{12} (GPa)	G_{13} (GPa)	G_{23} (GPa)	ν_{12}
103	6.7	2.7	2.7	2.5	0.34

$$G_C = G_{IC} + [G_{IIC}(v) - G_{IC}]\left(\frac{G_{II}}{G_T}\right)^{\eta} \tag{5}$$

It is to note that to fit the experimental data, G_{IC} is fixed at 245 N/m (obtained at 1 mm/min) [24] and $G_{IIC}(v)$ is a function of displacement rate as described by Eq. (4). The surface fit is performed on the experiment data to find the best coefficient η value in Eq. (5). For optimization, a nonlinear least-squares fitting method based on trust region is used [38]. Fig. 6 shows the surface fit with the best-fit material parameter $\eta = 3.175$.

Table 1 shows the experimental fracture toughness, curve fit fracture toughness and their deviation. The experimental fracture toughness is measured with the mode ratio from 0 to 1 and displacement rate in logarithmic scale from 0 to 6.2, whereas the curve fit fracture toughness is obtained from Eq. (5). The absolute percentage deviation of fracture toughness is obtained through Eq. (6).

$$\Delta FT = \left|\frac{FT_c - FT_e}{FT_e}\right| \times 100\% \tag{6}$$

where ΔFT is the absolute percentage deviation of the fracture toughness, FT_c is curve fit fracture toughness and FT_e is experimental fracture toughness. The average ΔFT of 7% indicates the accuracy of Eq. (5) in predicting the fracture toughness.

5. Numerical modelling

5.1. Finite element model

Fig. 7 illustrates the finite element model of a SLB test specimen. The specimen is simply supported with a vertical displacement applied at the mid-span. To ensure consistency, the same modelling approach used in the authors previous studies is implemented [24,25,39]. Continuum shell elements (SC8R) are used for the composite arms, with the lamina properties listed in Table 2. The lamina properties were determined in the authors' previous studies and have been successfully implemented in modelling the mode I [24] and mode II [25] delamination of the same carbon/epoxy composite. Cohesive elements (COH3D8) with a thickness of 10 μm are implemented along the mid-plane interface to simulate delamination propagation. A small thickness is imposed to avoid

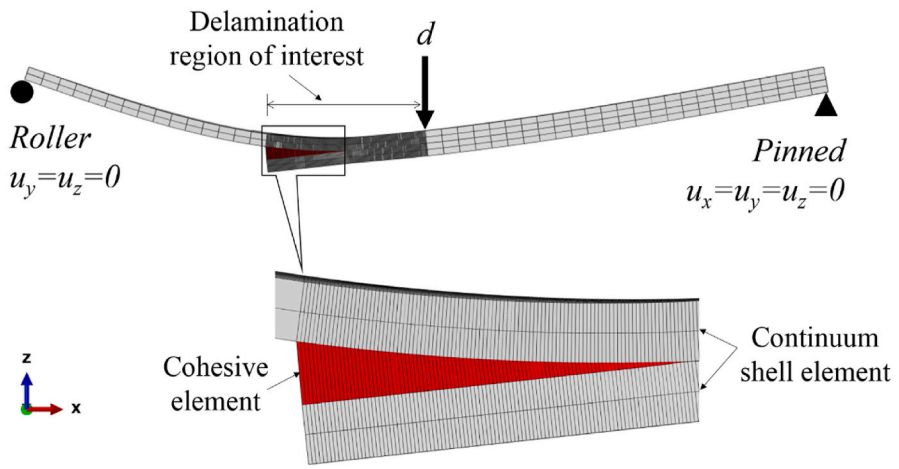

Fig. 7. Finite element model of the SLB specimen.

Table 3
Cohesive properties for the interface [24,25].

v (mm/min)	G_{IC} (N/m)	G_{IIC} (N/m)	$t_{u,n}$ (MPa)	$t_{u,s}$ (MPa)
1	245.03	1349.26	35	82
10	202.59	1795.78	35	104
100	275.06	1962.69	35	93
500	258.59	1623.85	35	88

interpenetration [40]. In addition, it is the same order of the resin-rich interface between the two adjacent laminas [41] and the thickness of the Teflon used in this study. Mollón et al. [42] have also used the same thickness to model the cohesive elements. This is also to ensure the consistency in the thickness that was used in the authors' previous studies on mode I [24] and mode II [25] delamination using the same composite material. The cohesive properties are listed in Table 3. To ensure the consistency in the modelling approach, the same cohesive parameters that have been used in the authors' previous studies for mode I [24] and mode II [25] delamination of the same composite are adopted. Both normal and shear interface stiffness are fixed at 4.5×10^5 N/mm^3 at all displacement rates [24,25]. In addition, the composite layers are discretised into a total of four elements in the thickness direction. The delamination region of interest meshed with a fine cohesive element size of 0.1 mm. The region outside the delamination region of interest meshed with a coarser element length of 2 mm. Uniform mesh of 0.5 mm mesh is used to discretise the model in the width direction. Damage initiation is governed by the quadratic nominal stress criterion (Eq. (7), where t indicates the traction and the subscript u refers to the interface strength. In addition, the subscripts n and s refer to normal (mode I) and shearing (mode II) modes, respectively. The symbol $\langle\cdot\rangle$ refers to the Macaulay bracket where no damage will be initiated under a compressive stress state. Delamination starts to occur at a material point of the interface when the quotient of the nominal stress ratios reaches unity. As for damage propagation, it is simulated using BK-criterion (Eq. (5)). It is to note that since the simulation is carried out separately for each displacement rate, the experimental fracture toughness values listed in Table 3 are used. Hence, in the below study, numerical simulation using the fitted values from Eq. (4) and Eq. (5) is not attempted. It is worth to note that for this modelling approach, the displacement rate effect is considered by inputting the different mode I and mode II fracture toughness values determined experimentally at each different rate. Since the penalty stiffness for mode I and mode II at all displacement rates is fixed based on the authors' previous findings on the same composite material [24,25], the interface strength could be estimated using Eq. (8) [43]. With this approach, when suitable mode I penalty stiffness and interface strength values are chosen [24], the mode II penalty stiffness and penalty strength could be directly estimated [25]. The implementation of Eq. (8) is also in accordance to May [44], where both interface strength and fracture toughness need to be considered for rate-dependency numerical simulation. This simple approach has been successfully implemented in pure mode I [24] and pure mode II [25] cases. To simulate the mixed-mode I/II delamination behaviour at different displacement rates, the same set of pure mode cohesive parameters (listed in Table 3) is implemented in this study without further calibration. The intention is to evaluate whether this approach is unified and suitable for both pure- and mixed-mode cases.

$$\left\{\frac{\langle t_n\rangle}{t_{u,n}}\right\}^2 + \left\{\frac{t_s}{t_{u,s}}\right\}^2 = 1 \tag{7}$$

$$t_{u,s} = \sqrt{\frac{G_{IIC}}{G_{IC}}}\, t_{u,n} \tag{8}$$

5.2. Numerical analyses

Fig. 8 compares the experimental and numerical force-displacement curves of the SLB specimens at 1, 10, 100, and 500 mm/min, respectively. Results indicate that the initial linear slopes are in good agreement with the experiments, with a maximum difference of 7%. This is an indication that the pure mode penalty stiffness used in previous studies [24,25] is still suitable for the mixed-mode case. Nevertheless, the peak load difference is relatively significant, ranging between 11 and 28%. In terms of average, the difference is 21%, 21%, 13% and 16% at 1, 10, 100 and 500 mm/min, respectively. It is worth noting that the same set of penalty stiffness, interface strength, and pure mode fracture toughness for pure mode I [24] and mode II [25] are used for mixed-mode delamination in this study.

In the previous studies, the same set of parameters was found to be able to well predict the numerical response of pure mode I and mode II cases, with a maximum of 2% and 10% of stiffness difference for mode I and mode II cases, respectively. As for the peak force, a maximum of 8% and 6% were reported for mode I and mode II cases. The possible reason of the relatively significant difference in the peak force for the mixed-mode case is due the difference in the experimental and numerical damage dissipated energy, which will be discussed in detail later.

Fig. 9 depicts the crack growth at different displacement rates when

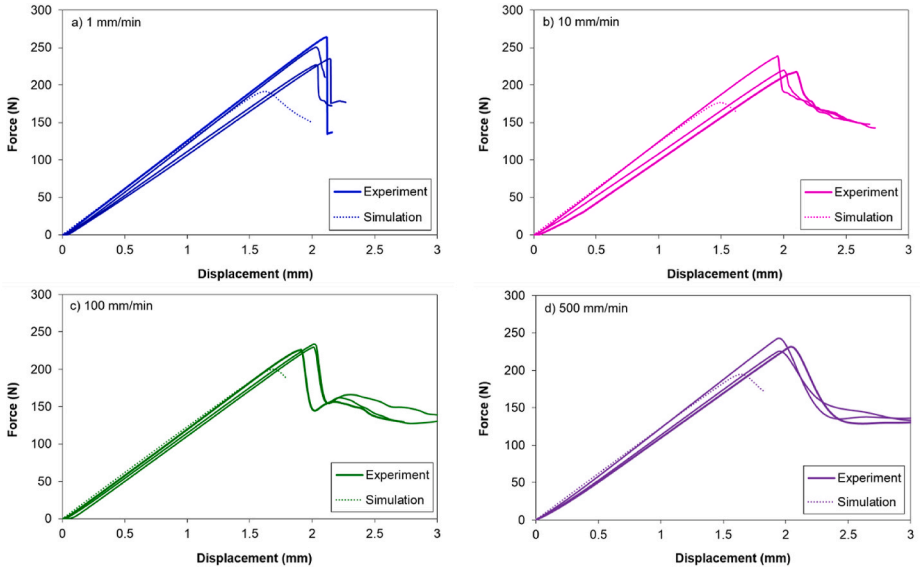

Fig. 8. Experimental and numerical force-displacement curves of the SLB specimens at (a) 1, (b) 10, (c) 100, and (d) 500 mm/min.

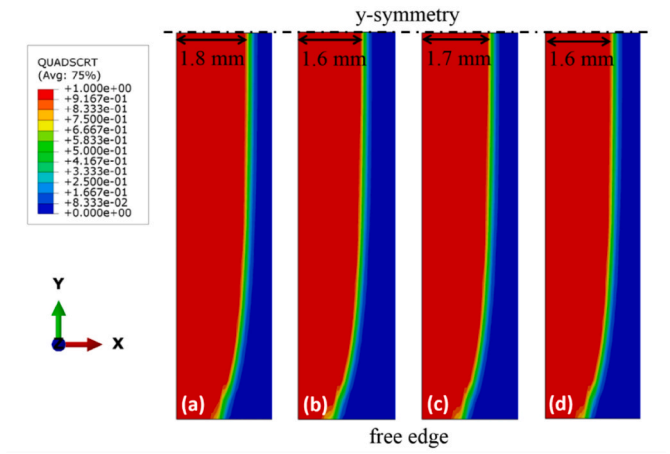

Fig. 9. Crack growth profile at the peak force at (a) 1, (b) 10, (c) 100, and (d) 500 mm/min.

the peak force is attained. The display output parameter QUADSCRT reaching 1 (shown in red in Fig. 9) indicates that the damage initiation criterion (Eq. (7)) of the cohesive element has been satisfied, where the element is experiencing damage degradation. Due to symmetry, only half of the width of the model is shown. The crack across the width shows a thumb-like pattern, where the crack grows slightly slower at the edge of the specimen. This is similar to the observation for the mode I case [24], however, it is opposite to what was reported for the mode II case [25].

At the peak load, the damage has been initiated and extended from the initial crack tip along the delamination path up to about 1.8, 1.6, 1.7, and 1.6 mm at a displacement rate of 1, 10, 100, and 500 mm/min, respectively. The similarity in the crack growth profile among the displacement rates is believed to be due to the closeness in the mixed-mode fracture toughness values.

Fig. 10 plots the theoretical and numerical traction-separation variations in mode I, mode II and mixed-mode I/II planes. Since the traction-separation response is similar among all four displacement rates, the two-dimensional plots for mode I, mode II and mixed-mode I/II at 1 mm/min are presented in Fig. 11 for illustration purposes. The pure modes (labelled as "Pure" in Fig. 11 (a) and (b)) are plotted based on the cohesive properties listed in Table 3. Since the penalty stiffness for both pure normal and shear modes is 4.5×10^5 N/mm^3 at all displacement rates, it would be the same for the mixed-mode case. The other parameters for theoretical mixed-mode traction-separation response (labelled as "Theoretical" in Fig. 11 (c)) based on BK-criterion are calculated as follows [43]:

For mixed-mode interface strength $t_{u,m}$,

$$t_{u,m} = \sqrt{t_{u,n}^2 + \left[t_{u,s}^2 - t_{u,n}^2\right]\left(\frac{G_{II}}{G_T}\right)^{\eta}} \tag{9}$$

For mixed-mode damage initiation separation $\delta_{o,m}$,

$$\delta_{o,m} = \sqrt{\delta_{o,n}^2 + \left[\delta_{o,s}^2 - \delta_{o,n}^2\right]\left(\frac{G_{II}}{G_T}\right)^{\eta}} \tag{10}$$

As for mixed-mode damage final separation $\delta_{f,m}$,

$$\delta_{f,m} = \frac{1}{\delta_{o,m}}\left[\delta_{o,n}\delta_{f,n} + \left(\delta_{o,s}\delta_{f,s} - \delta_{o,n}\delta_{f,n}\right)\left(\frac{G_{II}}{G_T}\right)^{\eta}\right] \tag{11}$$

Subsequently, the theoretical pure mode components (labelled as "Mixed" in Fig. 11 (a) and (b)) are calculated from the phase angle θ,

$$t_{u,I} = t_{u,m}\cos\theta, t_{u,II} = t_{u,m}\sin\theta \tag{12}$$

$$\delta_{o,I} = \delta_{o,m}\cos\theta, \delta_{o,II} = \delta_{o,m}\sin\theta \tag{13}$$

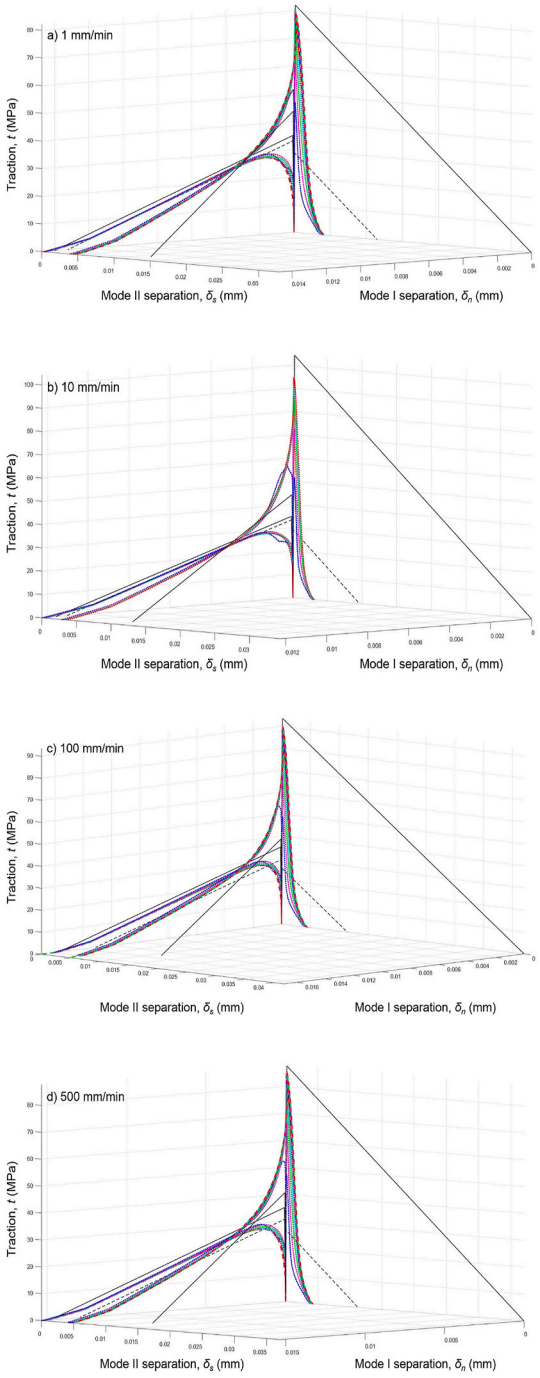

Fig. 10. Theoretical and numerical traction-separation responses at (a) 1, (b) 10, (c) 100, and (d) 500 mm/min.

$$\delta_{f,I} = \delta_{f,m}\cos\theta, \delta_{f,II} = \delta_{f,m}\sin\theta \tag{14}$$

The theoretical phase angle θ is calculated using:

$$\theta = \tan^{-1}\sqrt{\frac{G_{II}}{G_I}} \tag{15}$$

For SLB test, the theoretical mode ratio are $G_I/G_T = 0.57$ and $G_{II}/G_T = 0.43$, hence, the theoretical phase angle $\theta = 41°$. Table 4 lists all the mixed-mode and pure mode components of the theoretical traction and separation values by using the best-fit BK parameter $\eta = 3.175$.

Figs. 10 and 11 also plot the numerical traction-separation response of the first ten elements from the crack tip of mixed-mode and pure mode

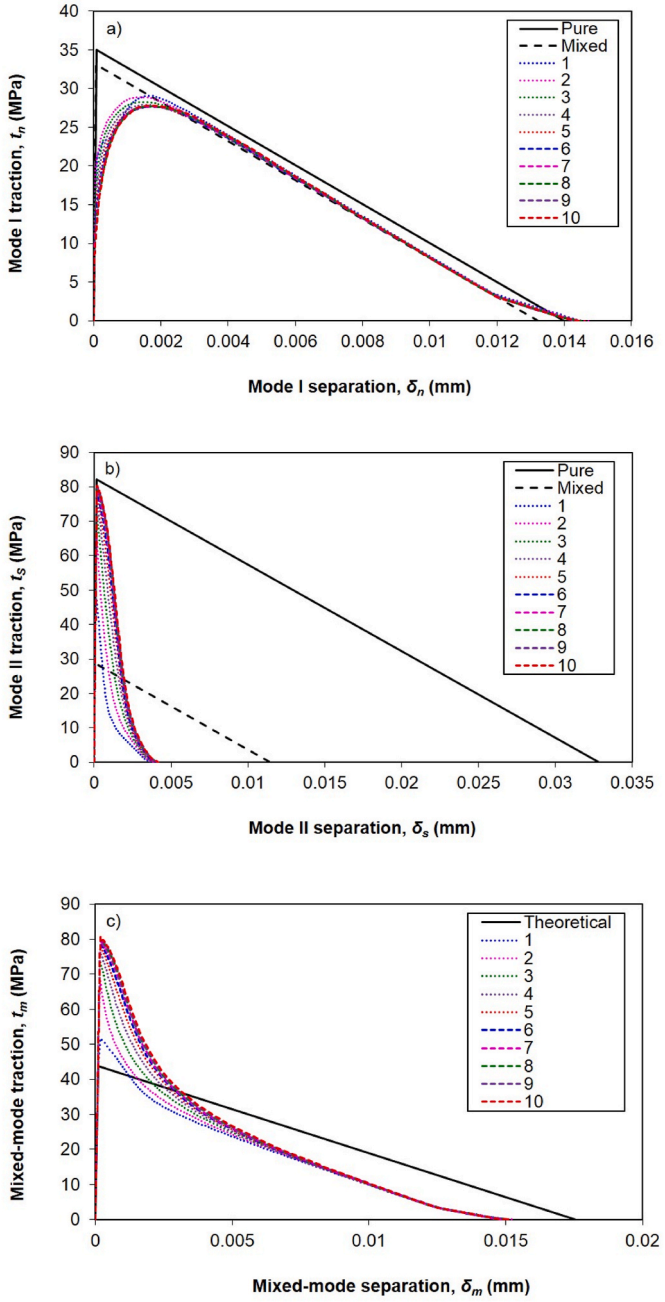

Fig. 11. Two-dimensional plots for (a) mode I, (b) mode II and (c) mixed-mode I/II at 1 mm/min.

components at different displacement rates. From both Fig. 11 and Table 4, it could be noticed that the interface strength of the mode II component $t_{u,II}$ is always smaller than the mode I component $t_{u,I}$, because the theoretical θ is less than 45°. In addition, it is also to note that the pure mode component ("Mixed") is always smaller than the pure mode input values ("Pure"), because "Mixed" is the component that is resolved from the mixed-mode resultant. For mode I component, Fig. 11 (a) shows that non-linearity is observed before the peak traction is achieved. Subsequently, the normal traction component decreases in the same trend as the theoretical traction-separation response. In addition, at each displacement rate, the numerical traction-separation response for all the ten elements is similar. As for mode II component, a significant difference is observed as compared to the theoretical traction-separation response. As seen in Fig. 11 (b), the numerical mode II peak traction is higher than the theoretical mode II component (labelled as "Mixed"). In addition, the value is in an increasing trend with respect to the distance from the crack-tip and converged towards the mode II interface strength (labelled as "Pure"). Upon the attainment of peak traction, the numerical mode II traction drops abruptly in a non-linear pattern, and the final mode II separation is attained at a value that is much smaller than the theoretical value.

Table 4
Theoretical traction and separation parameters for mixed-mode and pure mode components.

v (mm/min)		$t_{u,m}$ (MPa)		$\delta_{o,m}$ (mm)		$\delta_{f,m}$ (mm)
1		43.79		9.73×10^{-5}		1.75×10^{-2}
10		44.33		9.85×10^{-5}		1.47×10^{-2}
100		38.70		8.60×10^{-5}		1.74×10^{-2}
500		40.60		9.02×10^{-5}		1.71×10^{-2}
v (mm/min)	$t_{u,I}$ (MPa)	$\delta_{o,I}$ (mm)	$\delta_{f,I}$ (mm)	$t_{u,II}$ (MPa)	$\delta_{o,II}$ (mm)	$\delta_{f,II}$ (mm)
1	33.06	7.35×10^{-5}	1.32×10^{-2}	28.71	6.38×10^{-5}	1.15×10^{-2}
10	33.47	7.44×10^{-5}	1.11×10^{-2}	29.07	6.46×10^{-5}	0.96×10^{-2}
100	29.22	6.49×10^{-5}	1.31×10^{-2}	25.38	5.64×10^{-5}	1.14×10^{-2}
500	30.65	6.81×10^{-5}	1.29×10^{-2}	26.62	5.92×10^{-5}	1.12×10^{-2}

As for mixed-mode, the numerical traction-separation response is similar to the mode II component, where the peak traction is always larger than the theoretical value and increases when the element is further away from the crack tip. Beyond numerical peak traction, the traction decreases in a non-linear trend. Towards the end of the separation, the traction follows a similar trend as the theoretical one. Nevertheless, the final separation is smaller than the theoretical value.

The difference between the theoretical and numerical traction-separation response is postulated to be attributed to the difference in the definition of mixed-mode ratio. The theoretical mixed-mode ratio is determined using linear elastic fracture mechanics (LEFM) closed-form solution. This is also the mixed-mode ratio that is applied to the specimens during the experiment. On the other hand, the numerical mixed-mode ratio, which is also known as local mixed-mode ratio, is computed at each integration point of the cohesive elements [45]. Therefore, it is not constant and varies along the cohesive zone, which have been reported by some other researchers [45,46]. Further comparison in the variation of the local mixed-mode ratio will be discussed in the later section through the plots of phase angle.

The numerical phase angle $\theta = \delta_{II}/\delta_I$ is plotted in Fig. 12. It is apparent that the phase angle varies with the mixed-mode separation δ_m, which is obtained by Eq. (15). In addition, the phase angle also varies differently with a different element. This observation is different from the theoretical phase angle, where it is a constant with a value of 41°. Non-constant numerical phase angle was also reported by Harper et al. [46]. The reason is that the local mixed-mode ratio is not a constant [43,45,47].

$$\delta_m = \sqrt{\delta_I^2 + \delta_{II}^2} \tag{16}$$

Fig. 13 compares the experimental and numerical fracture energy. At all displacement rates, the first element has the lowest fracture energy and has the largest deviation compared to the experimental value, with 31, 18, 21, and 24% for 1, 10, 100, and 500 mm/min, respectively. This is believed to be the major reason that the numerical peak load is lower than the experimental value. Turon et al. [43] have also reported that it was the fracture energy that influenced the numerical peak load. When it is away from the crack tip, the numerical fracture energy is increased and converged. For 1 mm/min and 10 mm/min, the numerical fracture energy is always lower than the experimental value. For 100 mm/min, the numerical fracture energy surpasses the experimental value from the

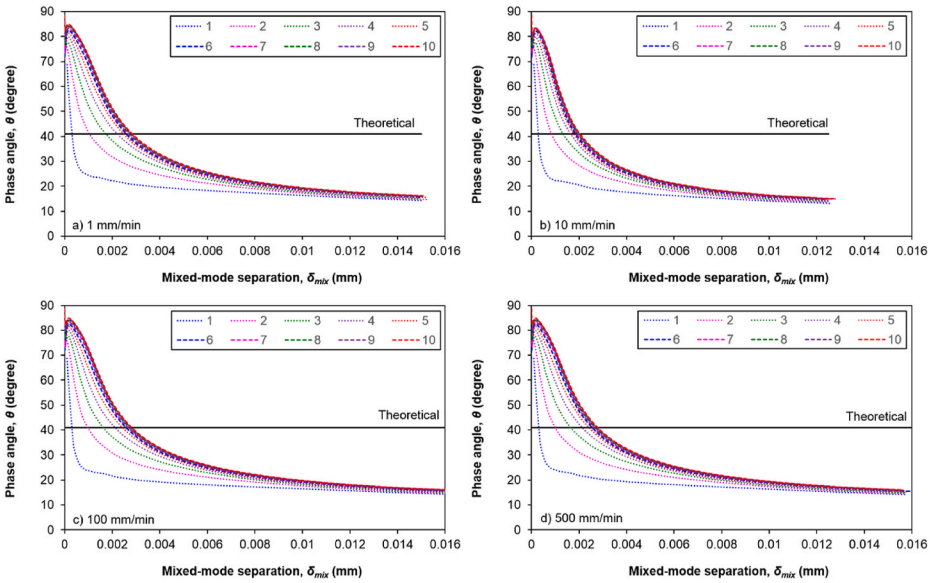

Fig. 12. Phase angle for the first ten elements from the crack tip at (a) 1, (b) 10, (c) 100, and (d) 500 mm/min.

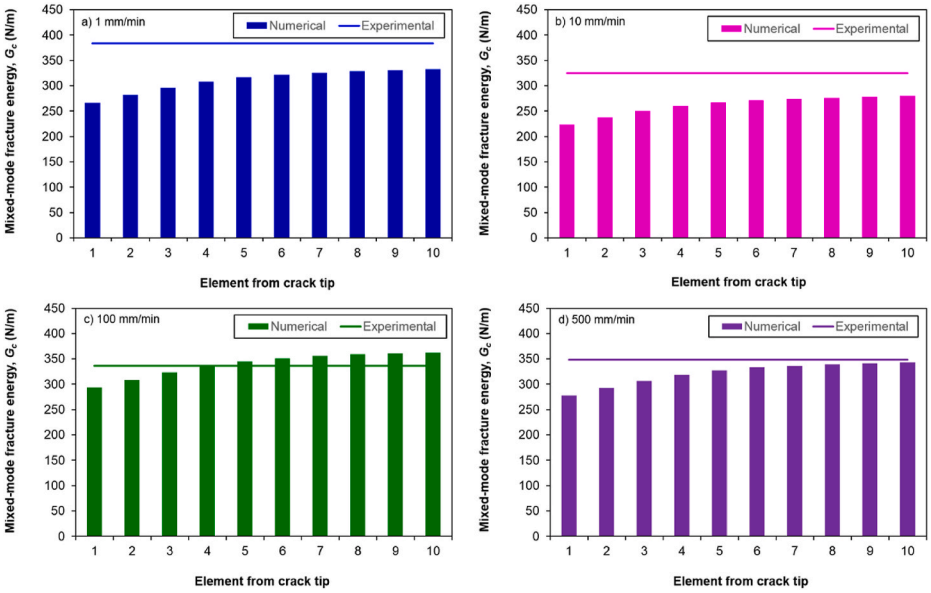

Fig. 13. Theoretical and numerical mixed-mode I/II fracture energy at (a) 1, (b) 10, (c) 100, and (d) 500 mm/min.

fourth element and onwards. It is reasonable to postulate that this is due to larger G_{IC} and G_{IIC} input values as compared to the other displacement rates (Table 3), thus more energy is dissipated during the numerical simulation. As for 500 mm/min, the numerical value converges towards the experiment value when the element is further away from the crack tip.

6. Conclusions

This research focuses on the experimental and numerical studies of mixed-mode I/II delamination of unidirectional carbon/epoxy composites at displacement rates of 1, 10, 100, and 500 mm/min. Mixed-mode I/II delamination was determined experimentally using single-leg bending (SLB) test, while a cohesive zone model was employed to simulate the delamination behaviour. Based on the results, it could be concluded that:

i. Mixed-mode I/II fracture toughness $G_{I/IIC}$ is invariant with the displacement rate. The average $G_{I/IIC}$ is 325–383 N/m within the speed of 1–500 mm/min.
ii. Surface morphology analyses show that shear cusps are more noticeable at 1, 10, and 100 mm/min, whereas significant matrix debris is observed at 500 mm/min.
iii. The three-dimensional rate-dependent fracture criterion is able to well predict the fracture toughness, with an average deviation of 7%.
iv. The numerical slope is well compared with the experimental value, with a maximum of 7% difference. However, the numerical peak load is lower than the experimental one, with a maximum difference of 21%. The reason is believed to be attributed to lower mixed-mode fracture energy dissipated during numerical simulation.
v. The theoretical and numerical traction-separation responses are obviously different for all mode I, mode II and mixed-mode I/II

cases. This observation is also reflected in the phase angle plots, where the numerical phase angle is varying with the mixed-mode separation. This is an indication of a non-constant local mixed-mode ratio.

Author statement

We would like to appreciate the editor and reviewers for their very useful and constructive comments. The manuscript has been modified/upgraded according to the editor and reviewer comments. The responses to the points raised by the reviewers are prepared in a separate file and attached.

As a general revision of the manuscript, we have gone through the manuscript text and revised it in terms of technical and language/grammatical points of view.

Declaration of competing interest

The authors declare that they have no known competing financial interests or personal relationships that could have appeared to influence the work reported in this paper.

Acknowledgments

K.J. Wong and M.N. Mohd Nasir acknowledge Universiti Teknologi Malaysia through UTMShine Grant No. 09G16 and UTM High Impact Research Grant No. 08G57. S.S.R.K. and M.P. acknowledge the Ministry of Education, Youth, and Sports of the Czech Republic and the European Union (European Structural and Investment Funds Operational Program Research, Development, and Education) in the framework of the project "Modular platform for autonomous chassis of specialized electric vehicles for freight and equipment transportation", Reg. No. CZ.02.1.01/0.0/0.0/16_025/0007293, as well as Universiti Putra Malaysia under Putra Grant No. GP/2018/9635100.

References

[1] K.J. Wong, et al., Moisture absorption effects on mode II delamination of carbon/epoxy composites, Polymers 12 (9) (2020) 2162.
[2] N.H. Nash, et al., The influence of hydrothermal conditioning on the Mode-I, thermal and flexural properties of Carbon/Benzoxazine composites with a thermoplastic toughening interlayer, Compos. Appl. Sci. Manuf. 76 (2015) 135–144.
[3] M. Johar, et al., Numerical simulation methodology for mode II delamination of quasi-isotropic quasi-homogeneous composite laminates, J. Compos. Mater. 51 (28) (2017) 3955–3968.
[4] M.R. Hosseini, F. Taheri-Behrooz, M. Salamat-talab, Mode I interlaminar fracture toughness of woven glass/epoxy composites with mat layers at delamination interface, Polym. Test. 78 (2019) 105943.
[5] M.R. Hosseini, F. Taheri-Behrooz, M. Salamat-talab, Mode II interlaminar fracture toughness of woven E-glass/epoxy composites in the presence of mat interleaves, Int. J. Adhesion Adhes. 98 (2020) 102523.
[6] S. Li, S.R. Reid, Z. Zou, Modelling damage of multiple delaminations and transverse matrix cracking in laminated composites due to low velocity lateral impact, Compos. Sci. Technol. 66 (6) (2006) 827–836.
[7] M. May, Measuring the rate-dependent mode I fracture toughness of composites – a review, Compos. Appl. Sci. Manuf. 81 (2016) 1–12.
[8] W.J. Cantwell, M. Blyton, Influence of loading rate on the interlaminar fracture properties of high performance composites - a review, Appl. Mech. Rev. 52 (6) (1999) 199–212.
[9] J.J.M. Machado, et al., Mode I fracture toughness of CFRP as a function of temperature and strain rate, J. Compos. Mater. 51 (23) (2016) 3315–3326.
[10] J.J.M. Machado, et al., Mode II fracture toughness of CFRP as a function of temperature and strain rate, Compos. B Eng. 114 (2017) 311–318.
[11] H. Zabala, et al., Loading rate dependency on mode I interlaminar fracture toughness of unidirectional and woven carbon fibre epoxy composites, Compos. Struct. 121 (2015) 75–82.
[12] H. Zabala, et al., Dynamic 4 ENF test for a strain rate dependent mode II interlaminar fracture toughness characterization of unidirectional carbon fibre epoxy composites, Polym. Test. 55 (2016) 212–218.
[13] S. Marzi, A. Rauh, R.M. Hinterhölzl, Fracture mechanical investigations and cohesive zone failure modelling on automotive composites, Compos. Struct. 111 (2014) 324–331.
[14] M. Colin de Verdiere, et al., Influence of loading rate on the delamination response of untufted and tufted carbon epoxy non crimp fabric composites: mode I, Eng. Fract. Mech. 96 (2012) 11–25.
[15] M. Colin de Verdiere, et al., Influence of loading rate on the delamination response of untufted and tufted carbon epoxy non-crimp fabric composites/Mode II, Eng. Fract. Mech. 96 (2012) 1–10.
[16] B.R.K. Blackman, et al., The failure of fibre composites and adhesively bonded fibre composites under high rates of test. Part I: mode I loading-experimental studies, J. Mater. Sci. 30 (23) (1995) 5885–5900.
[17] B.R.K. Blackman, et al., The failure of fibre composites and adhesively bonded fibre composites under high rates of test. Part III: mixed-mode I/II and mode II loadings, J. Mater. Sci. 31 (17) (1996) 4467–4477.
[18] B. Abdi, et al., Effect of strain-rate on flexural behavior of composite sandwich panel, in: Applied Mechanics and Materials, Trans Tech Publ, 2012.
[19] A. Esmaili, F. Taheri-Behrooz, Effect of cohesive zone length on the delamination growth of the composite laminates under cyclic loading, Eng. Fract. Mech. 237 (2020) 107246.
[20] R. Rafiee, S. Sotoudeh, A hysteresis cohesive approach for predicting mixed-mode delamination onset of composite laminates under cyclic loading: Part I, model development, Compos. Struct. 277 (2021) 114667.
[21] R. Rafiee, S. Sotoudeh, A hysteresis cohesive approach for predicting mixed-mode delamination onset of composite laminates under cyclic loading: Part II, numerical and experimental analyses, Compos. Struct. 277 (2021) 114668.
[22] R. Rafiee, S. Sotoudeh, A cohesive zone model for predicting the initiation of Mode II delamination in composites under cyclic loading, J. Reinforc. Plast. Compos. 40 (5–6) (2020) 179–192.
[23] M. May, S.R. Hallett, A combined model for initiation and propagation of damage under fatigue loading for cohesive interface elements, Compos. Appl. Sci. Manuf. 41 (12) (2010) 1787–1796.
[24] K.O. Low, et al., Mode I delamination behaviour of carbon/epoxy composite at different displacement rates, Compos. B Eng. 176 (2019) 107293.
[25] K.O. Low, et al., Displacement rate effects on the mode II shear delamination behavior of carbon fiber/epoxy composites, Polymers 13 (11) (2021).
[26] A.J. Smiley, R.B. Pipes, Rate effects on mode I interlaminar fracture toughness in composite materials, J. Compos. Mater. 21 (7) (1987) 670–687.
[27] G.R. Irwin, J.A. Kies, Critical energy rate analysis of fracture strength, Weld. J. Res. Suppl. 33 (1954) 193–198.
[28] W.J. Cantwell, The Influence of loading rate on the mode II interlaminar fracture toughness of composite materials, J. Compos. Mater. 31 (14) (1997) 1364–1380.
[29] M. Yasaee, et al., Strain rate dependence of mode II delamination resistance in through thickness reinforced laminated composites, Int. J. Impact Eng. 107 (2017) 1–11.
[30] N.H. Nash, T.M. Young, W.F. Stanley, The influence of a thermoplastic toughening interlayer and hydrothermal conditioning on the Mode-II interlaminar fracture toughness of Carbon/Benzoxazine composites, Compos. Appl. Sci. Manuf. 81 (2016) 111–120.
[31] B.D. Davidson, M. Kumar, M.A. Soffa, Influence of mode ratio and hygrothermal condition on the delamination toughness of a thermoplastic particulate interlayered carbon/epoxy composite, Compos. Appl. Sci. Manuf. 40 (1) (2009) 67–79.
[32] P. Compston, et al., The effect of matrix toughness and loading rate on the mode-II interlaminar fracture toughness of glass-fibre/vinyl-ester composites, Compos. Sci. Technol. 61 (2) (2001) 321–333.
[33] H. Maikuma, J.W. Gillespie, D.J. Wilkins, Mode II interlaminar fracture of the center notch flexural specimen under impact loading, J. Compos. Mater. 24 (2) (1990) 124–149.
[34] A.J. Smiley, R.B. Pipes, Rate sensitivity of mode II interlaminar fracture toughness in graphite/epoxy and graphite/PEEK composite materials, Compos. Sci. Technol. 29 (1) (1987) 1–15.
[35] Y. Zhao, et al., Delamination growth behavior of a woven E-glass/bismaleimide composite in seawater environment, Compos. B Eng. 106 (2016) 332–343.
[36] J. Bonhomme, et al., Fractography and failure mechanisms in static mode I and mode II delamination testing of unidirectional carbon reinforced composites, Polym. Test. 28 (6) (2009) 612–617.
[37] P. Compston, P.Y.B. Jar, P. Davies, Matrix effect on the static and dynamic interlaminar fracture toughness of glass-fibre marine composites, Compos. B Eng. 29 (4) (1998) 505–516.
[38] J.J. Moré, D.C. Sorensen, Computing a trust region step, SIAM J. Sci. Stat. Comput. 4 (3) (1983) 553–572.
[39] S. Koloor, A. Abdul-Latif, M.N. Tamin, Mechanics of composite delamination under flexural loading, in: Key Engineering Materials, Trans Tech Publ, 2011.
[40] B.F. Sørensen, S. Goutianos, T.K. Jacobsen, Strength scaling of adhesive joints in polymer–matrix composites, Int. J. Solid Struct. 46 (3–4) (2009) 741–761.
[41] A. Turon, et al., An engineering solution for mesh size effects in the simulation of delamination using cohesive zone models, Eng. Fract. Mech. 74 (10) (2007) 1665–1682.
[42] V. Mollón, et al., Finite element modelling of mode I delamination specimens by means of implicit and explicit solvers, Polym. Test. 31 (3) (2012) 404–410.
[43] A. Turon, et al., Accurate simulation of delamination growth under mixed-mode loading using cohesive elements: definition of interlaminar strengths and elastic stiffness, Compos. Struct. 92 (8) (2010) 1857–1864.
[44] M. May, Numerical evaluation of cohesive zone models for modeling impact induced delamination in composite materials, Compos. Struct. 133 (2015) 16–21.

[45] C. Sarrado, et al., Assessment of energy dissipation during mixed-mode delamination growth using cohesive zone models, Compos. Appl. Sci. Manuf. 43 (11) (2012) 2128–2136.

[46] P.W. Harper, L. Sun, S.R. Hallett, A study on the influence of cohesive zone interface element strength parameters on mixed mode behaviour, Compos. Appl. Sci. Manuf. 43 (4) (2012) 722–734.

[47] S. Koloor, et al., Fatigue damage of cohesive interfaces in fiber-reinforced polymer composite laminates, Compos. Sci. Technol. 183 (2019) 107779.